

# High-concentration planar microtracking photovoltaic system exceeding 30% efficiency

Jared S. Price<sup>1†</sup>, Alex J. Grede<sup>1†</sup>, Baomin Wang<sup>1†</sup>, Michael V. Lipski<sup>1</sup>, Brent Fisher<sup>2</sup>, Kyu-Tae Lee<sup>3</sup>, Junwen He<sup>4</sup>, Gregory S. Brulo<sup>5</sup>, Xiaokun Ma<sup>5</sup>, Scott Burroughs<sup>2</sup>, Christopher D. Rahn<sup>5</sup>, Ralph G. Nuzzo<sup>4</sup>, John A. Rogers<sup>3</sup> and Noel C. Giebink<sup>1\*</sup>

**Prospects for concentrating photovoltaic (CPV) power are growing as the market increasingly values high power conversion efficiency to leverage now-dominant balance of system and soft costs. This trend is particularly acute for rooftop photovoltaic power, where delivering the high efficiency of traditional CPV in the form factor of a standard rooftop photovoltaic panel could be transformative. Here, we demonstrate a fully automated planar microtracking CPV system <2 cm thick that operates at fixed tilt with a microscale triple-junction solar cell at >660X concentration ratio over a 140° full field of view. In outdoor testing over the course of two sunny days, the system operates automatically from sunrise to sunset, outperforming a 17%-efficient commercial silicon solar cell by generating >50% more energy per unit area per day in a direct head-to-head competition. These results support the technical feasibility of planar microtracking CPV to deliver a step change in the efficiency of rooftop solar panels at a commercially relevant concentration ratio.**

The economic landscape of photovoltaic (PV) power has fundamentally changed. Driven by manufacturing advances and economies of scale over the past decade, silicon and thin-film PV module costs have decreased dramatically, far outpacing balance of system and soft cost reductions. To a growing extent, solar panels are no longer the dominant cost of the power they produce<sup>1–3</sup>.

This previously enviable situation has renewed emphasis on the value of high efficiency since generating more power from a given system leverages its overall cost. Multijunction concentrating photovoltaics (CPV) have long been pursued as a practical path to achieve high efficiency, culminating to date in commercial CPV modules that are nearly twice as efficient as silicon and thin-film PV panels (CPV power conversion efficiency  $\eta_p > 35\%$  versus  $15 < \eta_p < 20\%$  typical of PV modules)<sup>1,3–5</sup>. Existing CPV systems, however, tend to be large (commercial systems are often larger than automobiles) and rely on precision, dual-axis rotational tracking, which is incompatible with deployment on rooftops and in constrained-space urban environments where a significant fraction of worldwide photovoltaic power is generated.

Various tracking-integrated CPV concepts are being explored to address this challenge, with the ultimate goal of realizing high-efficiency CPV in the form factor of a standard, fixed-tilt PV panel<sup>6–15</sup>. This is particularly demanding from an optical concentration standpoint, since the optical system must be very compact (that is, commensurate with typical PV panel thicknesses  $\lesssim 2$  cm) and operate efficiently (optical efficiency,  $\eta_{opt} > 0.8$ ) at high-concentration ratio (commonly defined as  $CR > 100$ , where CR is the ratio of concentrated to incident light intensities) over a wide range of incidence angles ( $\theta_{acc} = \pm 70^\circ$ ) to collect sunlight over an entire day. Supplementary Fig. 1 discusses the required angular acceptance. Catadioptric planar microtracking ( $\mu$ PT) systems based

on a laterally moving solar cell array have previously shown promise in this regard but have never been demonstrated at a fully operational level<sup>14</sup>.

Here we report a prototype  $\mu$ PT CPV system that operates with a triple-junction (3J) microscale photovoltaic ( $\mu$ PV) cell at  $CR > 660$  over a  $140^\circ$  full field of view with peak power conversion efficiency exceeding 30%. Implemented with a microcontroller and tested outdoors at latitude tilt in central Pennsylvania, the system generates 54% more energy per unit area over an entire day than an adjacent commercial Si solar cell with 17% power conversion efficiency. These results represent an important step toward the goal of high-efficiency tracking-integrated CPV in the form factor of a standard rooftop photovoltaic panel.

## High-gain planar microtracking concentration

Figure 1a illustrates the basic  $\mu$ PT optical system geometry, where a central glass sheet containing a  $\mu$ PV cell slides freely between a pair of planoconvex refractive and reflective optics, lubricated by index-matching oil. This catadioptric design folds the optical path and maintains a flat intermediate focal plane, resolving the usual Petzval curvature problem (where the focal spot degrades with increasing incidence angle)<sup>6–9</sup> to enable lateral microtracking over a wide range of incidence angles<sup>14</sup>. A complete panel would consist of top and bottom lenslet arrays matched to a corresponding array of  $\mu$ PV cells.

Based on recent work exploring the limits of planar tracking concentration<sup>16</sup>, this design adopts a low-dispersion N-BK10 glass top optic ( $n \approx 1.5$ ) in combination with a more dispersive, higher-refractive-index N-LASF31A bottom optic ( $n \approx 1.9$ ) that together help to mitigate chromatic dispersion in a manner analogous to an achromatic doublet. To minimize parasitic reflections, a broadband fluoropolymer antireflection coating<sup>17</sup> is applied to the top lens

<sup>1</sup>Department of Electrical Engineering, The Pennsylvania State University, University Park, Pennsylvania 16802, USA. <sup>2</sup>Semprius Inc., 4915 Prospectus Drive, Suite C, Durham, North Carolina 27713, USA. <sup>3</sup>Department of Materials Science and Engineering, University of Illinois at Urbana-Champaign, Urbana, Illinois 61801, USA. <sup>4</sup>Department of Chemistry, University of Illinois at Urbana-Champaign, Urbana, Illinois 61801, USA. <sup>5</sup>Department of Mechanical and Nuclear Engineering, The Pennsylvania State University, University Park, Pennsylvania 16802, USA. <sup>†</sup>These authors contributed equally to this work. \*e-mail: ncg2@psu.edu

surface and the plano surface of the bottom mirror is coated with a 110-nm-thick alumina layer to suppress reflections from the  $n = 1.5$  to  $n = 1.9$  internal index discontinuity; Supplementary Fig. 2 provides additional details of the optical system.

The optical performance of this concentrator is first characterized in the laboratory under collimated, broadband illumination from a supercontinuum laser to mimic low-divergence direct sunlight. The top and bottom lens elements are custom-turned aspheres and the sliding middle sheet consists of a 600  $\mu\text{m}$  square GaAs  $\mu\text{PV}$  cell, transfer-printed and sandwiched between a pair of 0.5-mm-thick glass wafers. In this case, the geometric gain ( $G$ ) given by the ratio of the concentrator aperture area ( $A_{\text{conc}}$ , defined by the 20 mm lens diameter) to the cell area ( $A_{\text{cell}}$ ), is  $G = A_{\text{conc}}/A_{\text{cell}} = 873$ .

Figure 1b displays the optical efficiency measured as a function of incidence angle, where  $\eta_{\text{opt}} = P_{\text{cell}}/P_{\text{conc}}$  is defined as the fraction of optical power incident on the concentrator ( $P_{\text{conc}}$ ) that reaches the surface of the PV cell ( $P_{\text{cell}}$ ) in the supercontinuum wavelength range absorbed by GaAs ( $400 < \lambda < 873$  nm). The concentration ratio follows simply as the product of optical efficiency and geometric gain,  $\text{CR} = G\eta_{\text{opt}}$ . A single-junction cell is used in this measurement to avoid errors that might arise from sub-cell current mismatch in a multijunction PV cell. The results show that  $\eta_{\text{opt}}$  exceeds  $\sim 90\%$  for incidence angles up to  $70^\circ$ , in agreement with a ray-tracing simulation carried out in Zemax OpticStudio (purple solid line).

Based on this validation, the ray-tracing model is subsequently extended over a larger wavelength range ( $350 < \lambda < 1,850$  nm) to predict the optical efficiency for a 650  $\mu\text{m}$  square multijunction cell, which is used in the CPV system detailed below ( $G = 743$ , blue solid line). The similarity of this result to that for GaAs showcases the broadband nature of the concentrator, which in turn permits full spectrum concentration for three-, four- or five-junction PV cells<sup>18–20</sup>. This remarkable combination of optical efficiency, geometric gain, spectral bandwidth and acceptance angle far surpasses that of any previous  $\mu\text{PT}$  concentrator<sup>7,14,15</sup> and even rivals that of conventional, rotationally tracked CPV concentrators<sup>5,21</sup>.

## CPV system testing

The same optics are implemented in a complete, small-scale  $\mu\text{PT}$  CPV system shown in Fig. 2a. The testing jig shown in the photograph of Fig. 2a is designed to hold the top and bottom lens elements in place while sliding the glass wafer middle sheet laterally between them with a pair of motorized linear translation stages. The  $\mu\text{PV}$  cell in this case (shown in the inset of Fig. 2b) is a 650  $\mu\text{m}$  square InGaP/GaAs/InGaAsNSb 3J stack with corresponding bandgaps of 1.9, 1.4 and 1.0 eV. This cell architecture reaches approximately 42% power conversion efficiency at  $\text{CR} \approx 600$  as reported previously<sup>19</sup>. Closed-loop tracking control is provided by a microcontroller running a simple hill-climbing algorithm based on feedback from the  $\mu\text{PV}$  short-circuit current (details of the algorithm are provided in Supplementary Fig. 3). To provide several reference points for evaluation of the CPV performance, a bare 3J  $\mu\text{PV}$  cell, a 17%-efficient commercial Si solar cell, and a cosine-corrected pyranometer are mounted on the same testing jig (see Fig. 2a).

The entire assembly was subsequently taken to the National Oceanic and Atmospheric Administration (NOAA) Surface Radiation (SURFRAD) monitoring site near State College, Pennsylvania<sup>22</sup>, and tested outdoors facing south at latitude tilt ( $\sim 41^\circ$ ) as shown in Fig. 2c. The SURFRAD site provides a detailed breakdown of the surface radiation budget, including direct normal (DNI), diffuse and global horizontal irradiance parameters that are used to evaluate power conversion efficiency. Supplementary Fig. 4 provides a complete description of the test site. Figure 2d presents the SURFRAD irradiance conditions for a day-long test run conducted on 7 November 2016, broken down into diffuse, DNI and cosine-corrected DNI incident on the plane of the (latitude-tilted) CPV system. Accounting for the system orientation, the SURFRAD data

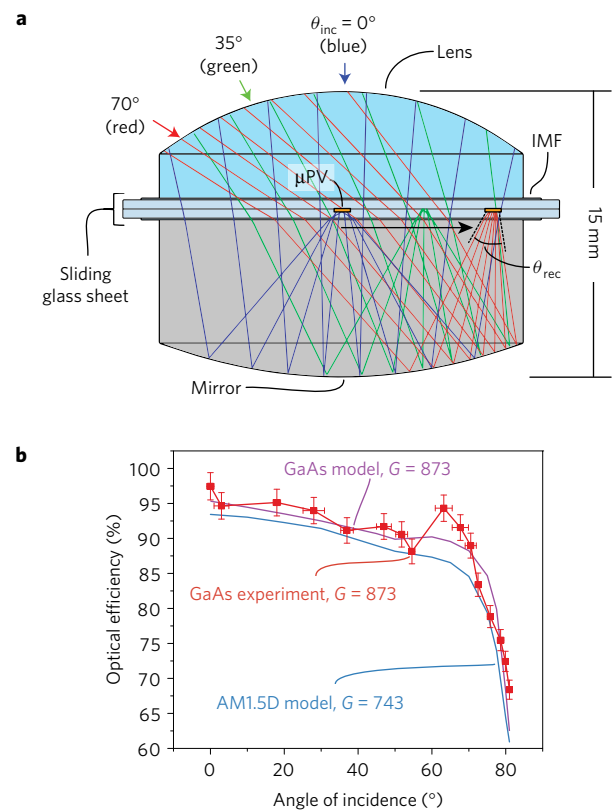


**Figure 1 | High-concentration planar microtracking.** **a**, Ray-tracing diagram of the concentrator optical system. The  $\mu\text{PV}$  cell is sandwiched between a pair of glass wafers bonded with optical adhesive and tracking is accomplished by sliding this composite middle sheet between planoconvex top and bottom lenses to align with the focal spot at different solar incidence angles. The sliding middle sheet is lubricated with index-matching fluid (IMF) to reduce parasitic reflection losses within the concentrator stack. **b**, Optical efficiency measured for the concentrator as a function of incidence angle. The red data points are recorded under collimated, broadband illumination from a supercontinuum laser using a 600  $\mu\text{m}$  square GaAs  $\mu\text{PV}$  cell (corresponding to  $G = 873$ ); error bars reflect the uncertainty estimated from maximum and minimum values of independent measurements recorded on several different days. Solid lines are the result of ray-tracing simulations for the experimentally measured arrangement (600  $\mu\text{m}$  cell with supercontinuum wavelengths  $400 < \lambda < 873$  nm limited by the GaAs bandgap; purple line) and extended to the case of a 650  $\mu\text{m}$  square cell operating over the majority of the AM1.5D solar spectrum ( $350 < \lambda < 1,850$  nm; blue line).

collectively agree with the global irradiance recorded by the pyranometer mounted on the testing jig.

Figure 2e displays the CPV short-circuit current density together with that for the bare 3J  $\mu\text{PV}$  over the course of the day. The current enhancement ratio between the two ( $J_{\text{CR}}/J_0$ , shown on the right-hand scale) is  $\sim 570\times$  over the majority of the day, which is lower than the optical concentration ratio  $\text{CR} = G\eta_{\text{opt}} = 660$  calculated from Fig. 1b due to diffuse light capture by the bare cell (which inflates the denominator of the current enhancement ratio) as well as sub-cell current mismatch introduced by the spectral response of the concentrator; details are provided in Supplementary Fig. 5. The asymmetry in the current enhancement ratio over the course of the day results from a slight, inadvertent westward tilt of the bare cell relative to the plane of the testing jig, which causes its current to be lower in the morning and higher in the afternoon, leading to an artificial increase and decrease in the current enhancement ratio, respectively.

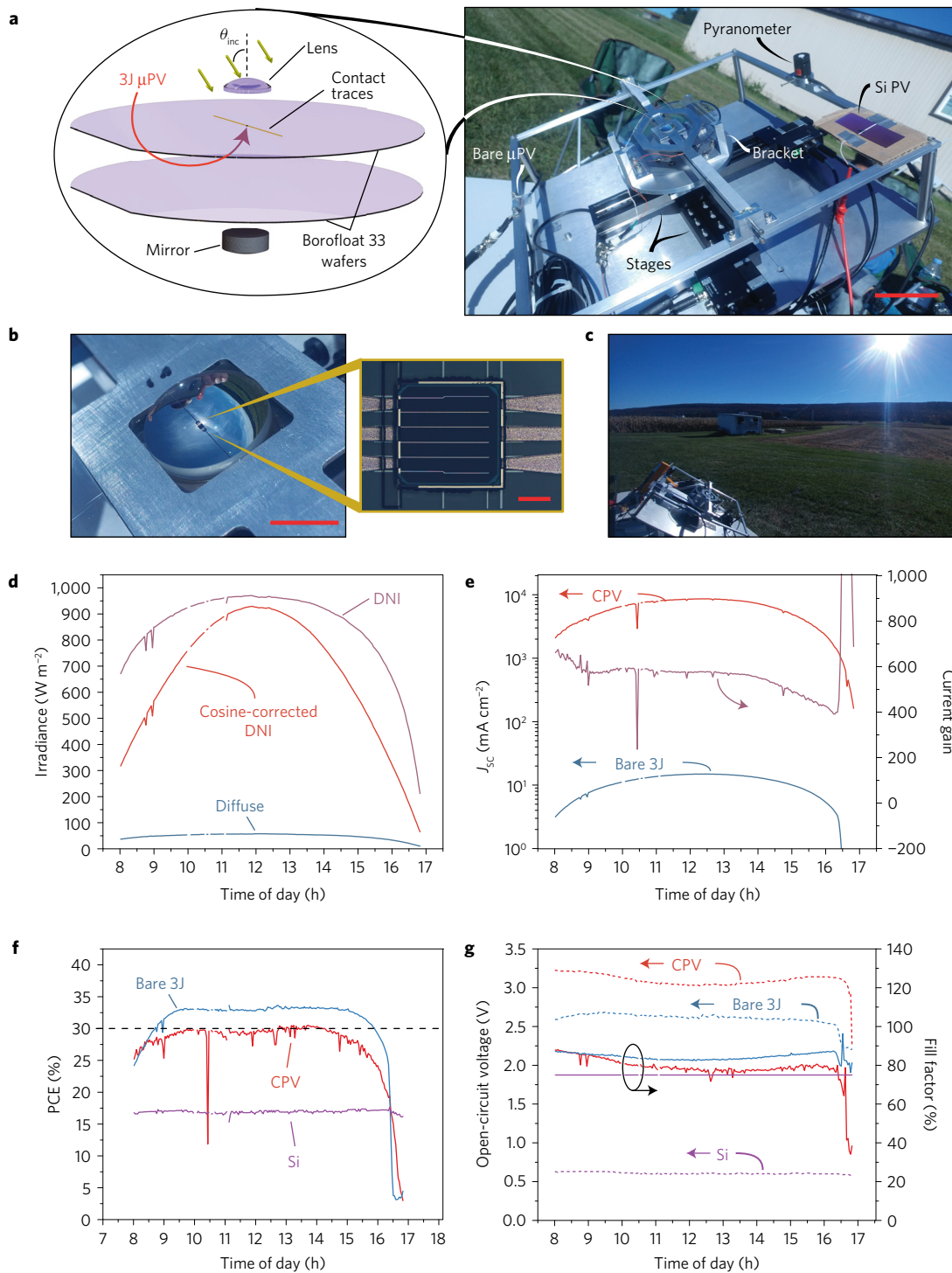


**Figure 2 | Outdoor testing results.** **a**, Photograph of the CPV testing jig. The lens and mirror optics shown in the blow-up diagram on the left are held by two fixed cross-members in the centre of the photograph while the glass wafer stack sandwiching the  $\mu$ PV cell is controlled by a surrounding bracket that moves laterally on top of a pair of crossed linear stages. The reference Si cell and pyranometer are located at the top of the jig while the bare 3J  $\mu$ PV is located at the bottom. The red scale bar in the photograph is 10 cm. **b**, Photograph showing a close-up view of the CPV optical system, with a picture of a typical 3J  $\mu$ PV cell shown in the inset (the red scale bars are 1 cm and 200  $\mu$ m, respectively). **c**, Photograph of the entire system being tested at the NOAA SURFRAD site. **d**, Direct (purple) and diffuse (blue) components of the solar irradiance together with the cosine-corrected direct component (red) incident on the oriented testing jig during the outdoor test on 7 November 2016. The Sun was obscured prior to  $\sim$ 8:00 by the ridge seen in the background of the photograph in **c**. **e**, Short-circuit current density,  $J_{sc}$ , for the CPV (red) and bare  $\mu$ PV (blue) cells along with their ratio (purple) shown on the right-hand axis. The geometric gain is  $G = 743$ . **f**, Power conversion efficiency (PCE) for the CPV (red), bare  $\mu$ PV (blue) and Si commercial cells (purple). The CPV efficiency is calculated relative to the direct irradiance whereas the unconcentrated cell efficiencies are referenced to the total irradiance. **g**, Open-circuit voltage (dashed lines, left axis) and FF (solid lines, right axis) for the CPV and bare reference cells; the colour coding is the same as for the previous plot. The midday reduction in both  $V_{oc}$  and FF for the CPV system results primarily from cell heating that follows the cosine-corrected irradiance incident on the concentrator in **d**.

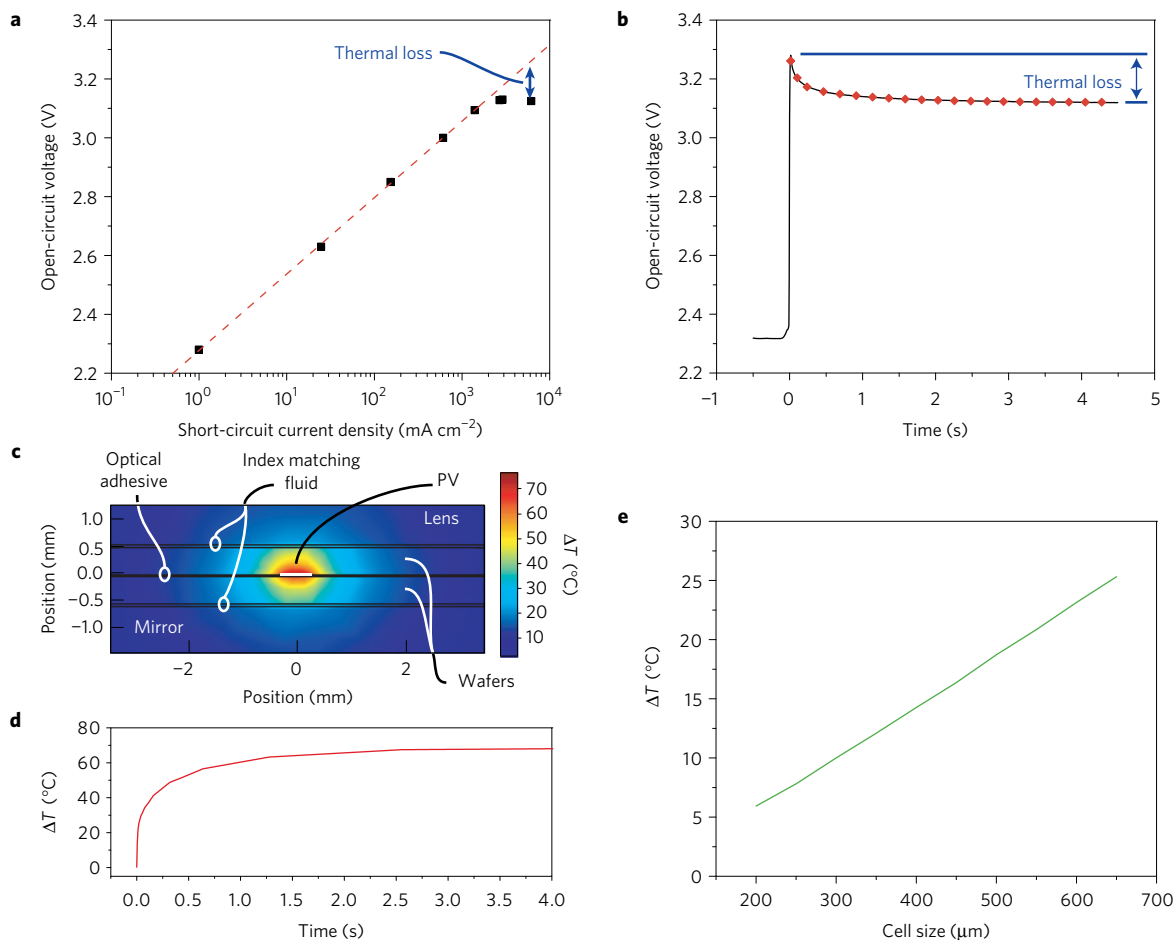


**Figure 3 | Microcell heating analysis.** **a**, Light intensity dependence of the CPV open-circuit voltage ( $V_{oc}$ ) recorded outdoors by placing a variable aperture in front of the concentrator lens. The dashed red line denotes the expected logarithmic dependence on short-circuit current density described in the text. The data deviate from this relationship at current densities  $>1 \text{ A cm}^{-2}$  due to cell heating. **b**, Transient  $V_{oc}$  measurement in which the CPV system was abruptly exposed to direct sunlight at  $t = 0$ . The data are shown in black, and red diamonds denote a biexponential fit as described in the text. **c**, Finite-element model showing the steady-state temperature increase above ambient,  $\Delta T$ , predicted within the experimental CPV system at open circuit under full sun illumination assuming all of the power is dissipated as heat. **d**, Model prediction of the transient change in average cell temperature above ambient following the onset of illumination. **e**, Simulated dependence of the average steady-state cell temperature increase versus square  $\mu\text{PV}$  cell side length at CR = 360 assuming maximum power point operation.

Figure 2f displays the power conversion efficiency for the CPV, bare 3J  $\mu\text{PV}$  and commercial Si cells. The efficiency for the unconcentrated 3J  $\mu\text{PV}$  and Si PV cells is calculated on the basis of the direct and diffuse irradiance incident on the cell area whereas the CPV efficiency is based only on the direct component incident on the concentrator per standard test practice<sup>5,21</sup>. The resulting CPV efficiency fluctuates near 30% from roughly 10:00 to 14:00 and remains above the 17% Si reference cell for virtually the entire day.

The fact that the CPV efficiency is lower than the unconcentrated 3J  $\mu\text{PV}$  cell attests to undesirable loss in both fill factor (FF) and open-circuit voltage ( $V_{oc}$ ) as shown in Fig. 2g. There, the CPV open-circuit voltage decreases by  $\sim 200 \text{ mV}$  from 8:00 to 13:00 despite a nearly fourfold increase in  $J_{sc}$  over the same time period that would nominally have been expected to yield a  $\sim 150 \text{ mV}$  increase based on the ambient temperature and cell ideality factor. The CPV FF exhibits a similar trend, decreasing from  $\text{FF} \approx 0.85$  at 8:00 to  $\text{FF} \approx 0.79$  at 13:00. All of the observations in Fig. 2 are reproduced in another day-long test conducted on 5 November 2016 and provided in Supplementary Fig. 6.

### Thermal management

The midday drop and partial late afternoon recovery of both  $V_{oc}$  and FF in the CPV system result mainly from cell heating. Evidence for

this conclusion follows from Fig. 3a, which demonstrates a deviation in the logarithmic scaling of  $V_{oc}$  on light intensity above a short-circuit current density of  $\sim 1 \text{ A cm}^{-2}$ . Cell heating is similarly supported by the transient decay of  $V_{oc}$  following sudden illumination by direct sunlight shown in Fig. 3b. The  $V_{oc}$  transient itself is empirically well described by a biexponential decay with time constants  $\tau_1 \sim 92 \text{ ms}$  and  $\tau_2 \sim 970 \text{ ms}$ . Given that the thermal conductivity of the semiconductor  $\mu\text{PV}$  cell is roughly one order of magnitude higher than that of the glass and adhesive surrounding the cell, it seems likely that  $\tau_1$  reflects the time constant of the cell itself whereas  $\tau_2$  reflects slower diffusion of heat into its surroundings.

Figure 3a,b clearly demonstrates cell heating but cannot be used as a direct measure of the temperature increase that occurs in Fig. 2g because the data sets are collected on different days under different irradiance conditions. Nevertheless, on the basis of the  $V_{oc}$  temperature coefficient for our 3J  $\mu\text{PV}$  cells,  $\beta = -4.7 \text{ mV } ^\circ\text{C}^{-1}$  (that is, the change in open-circuit voltage due to a given change in temperature), we can estimate the cell temperature rise in Fig. 2g via the usual light intensity and temperature relationship<sup>23</sup>,  $V_{oc} = V_{oc0} + \beta(T - T_0) + [nk_b T/q] \ln(J_{sc}/J_{sc0})$ . In this expression,  $n = 4.4$  is the  $\mu\text{PV}$  cell ideality factor,  $T$  is its temperature at a given short-circuit current density,  $J_{sc}$ , and  $V_{oc0}$ ,  $J_{sc0}$  and  $T_0$  refer to the same parameters when the cell is operated at a lower illumination intensity and/or

temperature reference point. Using the first measurements of the morning from Fig. 2 at 8:00 to establish this reference point when cell heating is assumed to be negligible, we find that the maximum cell temperature at midday exceeds the ambient by approximately 70 °C. Current–voltage measurements recorded from an identical  $\mu$ PV cell on a hot plate under 1 sun illumination indicate that this temperature rise is also partially responsible for the FF reduction observed in Fig. 2g; the balance is due to series resistive loss from the extended contact traces (shown in Fig. 2a) that manifests at high current.

Finite element simulations provide a basis to better understand heat rejection within the concentrator environment as well as opportunities to improve it. Figure 3c shows the steady-state temperature profile simulated for the CPV system under full sun illumination at open circuit, in agreement with the  $\sim 70$  °C heating estimated above. The transient rise in average cell temperature en route to this steady-state distribution is displayed in Fig. 3d and qualitatively agrees with the experimental transient in Fig. 3b insofar as it reproduces the biexponential form of the data with comparable magnitude fast ( $\tau_1 \sim 13$  ms) and slow ( $\tau_2 \sim 560$  ms) time constants that mark equilibration of the cell and surroundings, respectively. Although the highly localized nature of the temperature increase in Fig. 3c is undesirable from a cell cooling standpoint, it also means that the majority of the concentrator optic is not heated and thus thermal expansion and refractive index change have a minimal impact on the concentrator optical performance.

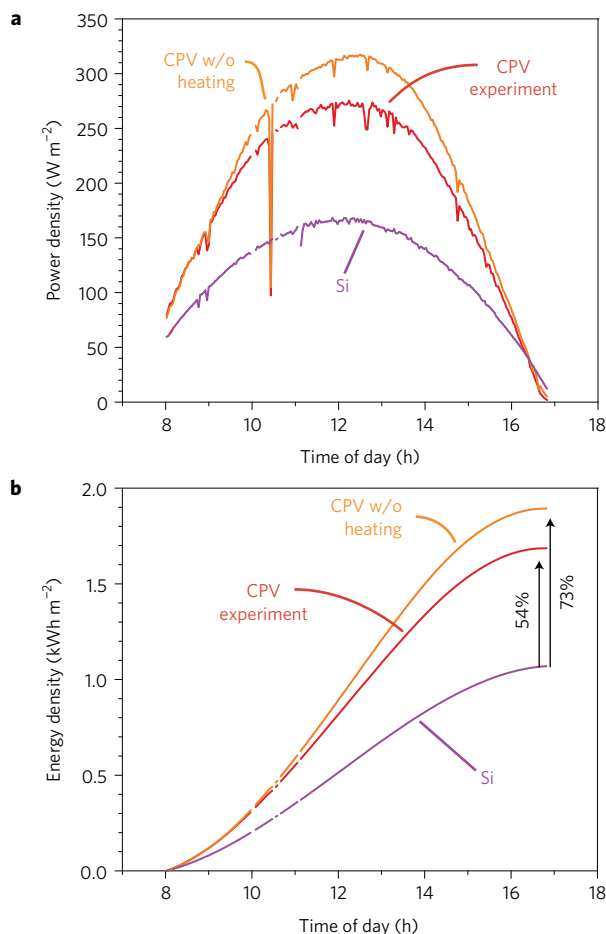
Moving forward, there is reason to believe that cell heating can be managed even without increasing the thermal conductivity of the middle sheet. At a trivial level, the heat load on the cell is naturally reduced by  $\sim 40\%$  when the cell operates delivering power at its maximum power point. In addition, because the refractive index of commodity optical glasses and plastics is lower than  $n \sim 1.6$ , the concentration ratio of an actual  $\mu$ PT CPV panel is probably limited to  $CR \sim 400$  (ref. 16). Relative to the present CPV system, these two changes together would reduce the cell heat load by roughly a factor of three.

Figure 3e shows that scaling to smaller  $\mu$ PV cells is also expected to yield a significant reduction in cell temperature. This follows from the increase in perimeter to area ratio with decreasing cell size and is a well-known benefit of operating with microscale photovoltaics under concentration<sup>20,24</sup>. In the present context, Fig. 3e predicts that, for maximum power point operation at  $CR = 360$ , a  $\mu$ PV cell size less than  $300 \times 300 \mu\text{m}^2$  will limit the temperature rise of the cell to  $< 10$  °C, which would largely eliminate the  $V_{oc}$  and FF losses observed in Fig. 2g.

The most direct, and arguably most important, comparison between the CPV system and the benchmark Si cell is simply the power generated per unit area shown in Fig. 4a. Whereas the Si cell power density peaks at  $\approx 170 \text{ W m}^{-2}$  in accord with its 17% AM1.5G efficiency, the CPV system peaks at  $\approx 275 \text{ W m}^{-2}$ , which is slightly lower than that expected from its nominal (DNI-based) 30% efficiency since it does not convert the small diffuse irradiance component in Fig. 2d. Nevertheless, integrated over the entire day, the CPV system delivers a total energy density of  $\sim 1.7 \text{ kW-h m}^{-2}$ , which is 54% higher than that produced by the Si cell as shown in Fig. 4b. If the heating-related  $V_{oc}$  and FF losses in the CPV system can be corrected as per Fig. 3e, the energy density enhancement over Si increases to more than 70% and the peak CPV power conversion efficiency reaches 35%.

## Discussion

The CPV system demonstrated here employs high-index glass to push the limits of  $\mu$ PV concentration in an intentional effort to uncover problems such as cell heating that arise at high flux. As noted above, however, the lower index of commodity optical glasses and plastics ( $1.5 \lesssim n \lesssim 1.6$ ) is likely to limit operation of a practical



**Figure 4 | Power and energy density.** **a**, Power per unit area generated by the CPV system (based on the concentrator area) and the commercial Si cell (based on the cell area) during the test on 7 November 2016. The orange line is a prediction based on the experimental data for the case in which the cell suffers no heating-related efficiency loss in  $V_{oc}$  or FF (that is, by using the early morning 8:00 data in Fig. 2g as a reference point, assuming that the FF remains constant throughout the day and  $V_{oc}$  scales logarithmically with the experimentally recorded  $J_{sc}$  as described in the text, but with  $\beta$  set to zero). **b**, Cumulative energy density obtained by integrating the power densities in **a** over time. The arrows show that the experimental CPV system generated 54% more energy than the commercial Si cell over the course of the day, and could have reached 73% more energy in the absence of cell heating losses.

$\mu$ PV panel to concentration ratios in the range  $300 < CR < 400$  without sacrificing the  $140^\circ$  angular acceptance<sup>16</sup>. This represents the lower bound in concentration ratio currently employed by commercial CPV systems<sup>4,5</sup>. Supplementary Figs 7–9 respectively detail the optical performance, manufacturing tolerances and operating temperature range for a large-scale lenslet array concentrator made of acrylic plastic.

Decreasing the  $\mu$ PV cell size at constant concentration ratio is expected to be beneficial on multiple accounts. Not only does it help mitigate cell heating (see Fig. 3e), but the associated size reduction of the concentrator optics reduces material usage, panel thickness and weight. Although scaling does increase the required tracking precision (the  $\mu$ PV positioning tolerance in the present system is roughly  $100 \mu\text{m}$ ; see Supplementary Fig. 10 for details), this is unlikely to be a problem for integrated  $\mu$ PT positioning approaches with  $\sim 1 \mu\text{m}$  precision described previously<sup>7</sup>.

Ultimately, the most important technical challenge facing  $\mu$ PT CPV is long-term reliability. There are numerous engineering

considerations involved in ensuring that such panels remain sealed and track every day without fail over a wide range of temperatures and weather conditions during a nominal 25-year lifespan. Supplementary Fig. 11 provides an example design for a complete module. In the most likely case of injection-moulded plastic concentrator optics, environmental degradation is an obvious concern, although field-proven acrylic CPV Fresnel lenses<sup>5,25,26</sup> and the introduction of durable, broadband antireflection coatings for plastic<sup>17</sup> provide cause for optimism.

Finally, as with any CPV system, the performance advantage of  $\mu$ PT CPV panels over standard PV relies on a high annual DNI level. Extending the experimental results in Fig. 4 to Phoenix, Arizona over the course of an entire year on the basis of the weather data and direct/diffuse breakdown available from the online calculator, PVWatts (<http://pvwatts.nrel.gov>), we predict that a  $\mu$ PT panel with no cell heating would deliver  $\sim 1.6\times$  more energy than a 17%-efficient Si panel of equal size. By contrast, the same calculation carried out in State College, Pennsylvania yields only a factor of  $\sim 1.3\times$  improvement.

## Conclusion

In summary, we report an automated planar microtracking CPV proof-of-concept system that achieves an unprecedented combination of efficiency ( $>30\%$  peak) and concentration ( $CR > 660$ ), resulting in  $>50\%$  more energy generated per unit area per day than a 17%-efficient commercial Si solar cell in head-to-head outdoor testing. Losses in both  $V_{oc}$  and FF due to cell heating under full sun illumination are collectively responsible for a 5% absolute efficiency decrease that can be avoided in the future by scaling to smaller cell sizes. If long-term reliability challenges can be addressed in a scalable panel design based on injection-moulded optics and transfer-printed  $\mu$ PV cells, the embedded CPV paradigm described here could offer a dramatic efficiency increase for rooftop photovoltaic power in sunny locations around the world.

## Methods

**Simulations.** Non-sequential ray-tracing simulations were carried out using Zemax OpticStudio accounting for all material absorption and optical constant dispersions, polarization-dependent Fresnel reflections, and thin-film-coating interference effects. The geometry of the concentrator stack was simulated and optimized over the AM1.5D solar spectrum in the  $350 < \lambda < 1,850$  nm spectral range accounting for the angular spread of the solar disk. Simulations of optical efficiency data measured in the laboratory account for the spectrum of the supercontinuum laser used as the illumination source.

Finite-element heat transfer modelling was conducted using COMSOL Multiphysics software assuming free convection and radiation on the outer optical surfaces and conduction for all internal interfaces in the concentrator stack. Power dissipation in the solar cell was modelled as a boundary heat source with a flux given by the optical power absorbed by the cell.

**Fabrication.** Single-junction GaAs  $\mu$ PV cells used for characterizing the concentrator optical performance were grown epitaxially and lifted off using an AlGaAs sacrificial layer as described previously<sup>14</sup>. Triple-junction InGaP/GaAs/InGaAsNSb cells were grown lattice-matched on a GaAs substrate and lifted off via an AlInP sacrificial layer as documented previously<sup>19</sup>. The total thickness of the cells is approximately 10  $\mu$ m and their surface is coated with a broadband TiO<sub>2</sub> (30 nm)/SiN<sub>x</sub> (45 nm)/SiO<sub>2</sub> (90 nm) antireflection coating that is designed for incidence from the surrounding glass. Individual cells were printed onto a 150 mm borofloat 33 glass wafer with photolithographically patterned contacts and subsequently encapsulated by bonding a second wafer on top with a  $\sim 30$ - $\mu$ m-thick layer of ultraviolet-curable optical adhesive (NOA 88, Norland).

The aspheric planoconvex top and bottom optics that make up the concentrator were custom-turned from N-BK10 and N-LASF31A glasses, respectively. The curved surface of the top lens is coated with a broadband antireflection coating via oblique-angle evaporation of Teflon AF (Chemours)<sup>17</sup>. Reflection loss within the concentrator stack at the interface with the high-index bottom optic is suppressed by depositing a 110-nm-thick Al<sub>2</sub>O<sub>3</sub> layer on its plano surface and the mirror coating applied to the curved bottom surface consists of SiO<sub>2</sub> (80 nm)/Al<sub>2</sub>O<sub>3</sub> (10 nm)/Ag (120 nm) with a protective Cu overlayer to prevent Ag oxidation. The complete concentrator was assembled by sandwiching the wafer stack containing the  $\mu$ PV cell between the top and bottom lenses held

in the testing jig (see Fig. 2a) using BK7 index-matching fluid (Cargille Labs) for lubrication.

**Experimental testing.** The concentrator optical efficiency was characterized in the laboratory using collimated light ( $<1^\circ$  divergence) from a broadband supercontinuum laser ( $400 < \lambda < 2,500$  nm, Fianium). The optical efficiency is determined via the ratio of the short-circuit current from a bare GaAs  $\mu$ PV cell ( $J_0$ ) to that measured from the same cell in the concentrator ( $J_{CR}$ ) according to  $\eta_{opt} = (J_{CR} T_{ac}) / (G J_0 (T_{cc})) K_{proj}$ . In this expression,  $G$  is the geometric gain,  $T_{ac}(\theta_{inc})$  is the spectrally averaged transmittance from air into the bare  $\mu$ PV cell at a given incidence angle,  $\theta_{inc}$ , and  $(T_{cc})$  is that from the concentrator glass into the cell averaged over the range of incidence angles,  $\theta_{cc}$  (see Fig. 1a), at the focal point. The geometric factor,  $K_{proj}$ , accounts for the reduced cosine projection loss experienced at high oblique incidence angles by the curved top lens of the concentrator stack as compared with the planar surface of the reference cell;  $K_{proj}$  deviates from unity only for  $\theta_{inc} > 60^\circ$ . A single-junction GaAs  $\mu$ PV is used as the reference cell in this measurement to avoid potential errors from sub-cell current mismatch in multijunction cells that are not tuned for the supercontinuum laser spectrum used in the measurement.

Current–voltage data were recorded using a pair of Keithley 2401 source-measure units for both indoor and outdoor measurements using four-point connections whenever possible to minimize series resistive losses. A four-point measurement was not available for the Si reference cell during the 7 November 2016 outdoor test (but was used on the 5 November 2016 test) and therefore, to avoid underestimating the FF of that cell due to series resistive loss, a constant representative FF = 0.78 is taken for it on this particular day. The CPV system was initialized at the start of each day by manually aligning the  $\mu$ PV wafer stack with the focal spot and then turning control over to an Arduino microcontroller programmed with a hill-climbing algorithm to optimize the cell position on the basis of feedback from the short-circuit current. The pyranometer mounted on the testing jig is a LI-200R (LI-COR) and the Si reference cell is a monocrystalline 156B3-200R (MOTEC) cut to  $76.2 \times 25.4$  mm<sup>2</sup> rectangular dimensions. The efficiency for the unconcentrated 3J  $\mu$ PV and Si PV reference cells is calculated on the basis of the NOAA SURFRAD direct and diffuse irradiance incident on the cell area whereas the CPV efficiency is based only on the direct component incident on the 20-mm-diameter concentrator area. The cosine-corrected DNI in each case is determined from the known orientation of the Sun relative to the testing jig according to the National Renewable Energy Laboratory Solar Position Algorithm<sup>27</sup>.

**Data availability.** The data that support the findings of this study are available from the corresponding author upon reasonable request.

Received 2 February 2017; accepted 13 June 2017; published 17 July 2017

## References

- Green, M. A. Commercial progress and challenges for photovoltaics. *Nat. Energy* **1**, 15015 (2016).
- Lewis, N. S. Research opportunities to advance solar energy utilization. *Science* **351**, 353 (2016).
- Woodhouse, M. et al. *On the Path to SunShot: The Role of Advancements in Solar Photovoltaic Efficiency, Reliability, and Costs* Tech. Rep. NREL/TP-6A20-65872 (2016).
- Philipps, S. P., Bett, A. W., Horowitz, K. & Kurtz, S. *Current Status of Concentrator Photovoltaic (CPV) Technology* Tech. Rep. NREL/TP-5J00-65130 (2015).
- Algora, C. & Rey-Stolle, I. *Handbook of Concentrator Photovoltaic Technology* Vol. 53 (John Wiley, 2016).
- Karp, J. H., Tremblay, E. J. & Ford, J. E. Planar micro-optic solar concentrator. *Opt. Express* **18**, 1122–1133 (2010).
- Hallas, J. M., Baker, K. A., Karp, J. H., Tremblay, E. J. & Ford, J. E. Two-axis solar tracking accomplished through small lateral translations. *Appl. Opt.* **51**, 6117–6124 (2012).
- Kotsidas, P., Modi, V. & Gordon, J. M. Nominally stationary high-concentration solar optics by gradient-index lenses. *Opt. Express* **19**, 2325–2334 (2011).
- Duerr, F., Meuret, Y. & Thienpont, H. Tracking integration in concentrating photovoltaics using laterally moving optics. *Opt. Express* **19**, A207–A218 (2011).
- Tremblay, E. J., Loterie, D. & Moser, C. Thermal phase change actuator for self-tracking solar concentration. *Opt. Express* **20**, A964 (2012).
- Zagolla, V., Tremblay, E. & Moser, C. Light induced fluidic waveguide coupling. *Opt. Express* **20**, A924 (2012).
- Duerr, F., Meuret, Y. & Thienpont, H. Tailored free-form optics with movement to integrate tracking in concentrating photovoltaics. *Opt. Express* **21**, A401–A411 (2013).

13. Zagolla, V., Tremblay, E. & Moser, C. Proof of principle demonstration of a self-tracking concentrator. *Opt. Express* **22**, A498 (2014).
14. Price, J. S., Sheng, X., Meulblok, B. M., Rogers, J. A. & Giebink, N. C. Wide-angle planar microtracking for quasi-static microcell concentrating photovoltaics. *Nat. Commun.* **6**, 6223 (2015).
15. Apostoleris, H., Stefanchich, M. & Chiesa, M. Tracking-integrated systems for concentrating photovoltaics. *Nat. Energy* **1**, 16018 (2016).
16. Grede, A. J., Price, J. S. & Giebink, N. C. Fundamental and practical limits of planar tracking solar concentrators. *Opt. Express* **24**, 1635–1646 (2016).
17. Wang, B., Price, J. S. & Giebink, N. C. Durable broadband graded-index fluoropolymer antireflection coatings for plastic optics. *Optica* **4**, 239–242 (2017).
18. King, R. R. *et al.* Solar cell generations over 40% efficiency. *Prog. Photovolt. Res. Appl.* **20**, 801–815 (2012).
19. Sheng, X. *et al.* Printing-based assembly of quadruple-junction four-terminal microscale solar cells and their use in high-efficiency modules. *Nat. Mater.* **13**, 593–598 (2014).
20. Lumb, M. P., Fisher, B., Schmieder, K. J. & Meitl, M. Six-junction (6J) microscale concentrating photovoltaics (CPV) for space applications. In *2016 IEEE 43rd Photovolt. Spec. Conf.* 3415–3420 (IEEE, 2016).
21. Luque, A. & Hegedus, S. S. *Handbook of Photovoltaic Science and Engineering* Ch. 10 (John Wiley, 2011).
22. ESRL Global Monitoring Division—Global Radiation Group (NOAA, accessed 8 November 2016); <https://www.esrl.noaa.gov/gmd/grad/surfrad/index.html>
23. Würfel, P. & Würfel, U. *Physics of Solar Cells: From Basic Principles to Advanced Concepts* (Wiley, 2016).
24. Ghosal, K. *et al.* Ultrahigh efficiency HCPV modules and systems. *IEEE J. Photovolt.* **6**, 1360–1365 (2016).
25. Miller, D. C. & Kurtz, S. R. Durability of Fresnel lenses: a review specific to the concentrating photovoltaic application. *Sol. Energy Mater. Sol. Cells* **95**, 2037–2068 (2011).
26. Miller, D. C. *et al.* An end of service life assessment of PMMA lenses from veteran concentrator photovoltaic systems. *Sol. Energy Mater. Sol. Cells* **167**, 7–21 (2017).
27. Reda, I. & Andreas, A. *Solar Position Algorithm for Solar Radiation Applications (Revised)* NREL/Tp-560-34302 (2008).

## Acknowledgements

This work was funded in part by the Advanced Research Projects Agency-Energy (ARPA-E) MOSAIC program, US Department of Energy, under Award No. DE-AR0000626 and by the National Science Foundation under Grant No. CBET-1508968. J.H. and R.G.N. were supported as part of the Department of Energy 'Light-Material Interactions in Energy Conversion Energy Frontier Research Center' under grant DE-SC0001293.

## Author contributions

J.S.P. designed and characterized the optics, designed the test jig for the CPV system, and performed the thermal simulations. A.J.G. wrote the outdoor testing software, and A.J.G. and M.V.L. wrote the tracking algorithm. B.W. designed and deposited all of the optical coatings and simulated the manufacturing and thermal tolerances of the system. Outdoor testing was carried out by all of the aforementioned authors. B.F. and S.B. supplied the 3J  $\mu$ PV cells for field testing, while K.-T.L., J.H., R.G.N. and J.A.R. supplied the GaAs  $\mu$ PV cells for concentrator optical efficiency measurements in the laboratory. G.S.B., X.M. and C.D.R. conceived the module design. N.C.G. supervised the project. J.S.P. and N.C.G. wrote the manuscript in consultation with all of the authors.

## Additional information

**Supplementary information** is available for this paper.

**Reprints and permissions information** is available at [www.nature.com/reprints](http://www.nature.com/reprints).

**Correspondence and requests for materials** should be addressed to N.C.G.

**How to cite this article:** Price, J. S. *et al.* High-concentration planar microtracking photovoltaic system exceeding 30% efficiency. *Nat. Energy* **2**, 17113 (2017).

**Publisher's note:** Springer Nature remains neutral with regard to jurisdictional claims in published maps and institutional affiliations.

## Competing interests

The authors declare that B.F., S.B. and J.A.R. (affiliated with Semprius) are involved in commercializing technologies related to those described here. J.A.R. is a co-founder of Semprius.